Supporting Information for "Multi-fault opposing-dip strike-slip and normal-fault rupture during the 2020 M_w 6.5 Stanley, Idaho earthquake"

Jidong Yang[1], Hejun Zhu[2], Thorne Lay[3], Yufeng Niu[4], Lingling Ye[5], Zhong Lu[6],

Bingxu Luo[2], Hiroo Kanamori[7], Jianping Huang[1], Zhenchun Li[1]

[1]Department of Geophysics, China University of Petroleum (East China), Qingdao 266580, China

[2]Department of Geosciences, The University of Texas at Dallas, Richardson, TX 75080, USA

[3]Department of Earth and Planetary Sciences, University of California, Santa Cruz, CA 95064, USA

[4]School of Mining and Geomatics Engineering, Hebei University of Engineering, Handan 056038, China

[5]Department of Earth and Space Sciences, Southern University of Science and Technology, Shenzhen, 518055, China

[6]Roy M. Huffington Department of Earth Sciences, Southern Methodist University, Dallas, TX 75205, USA

[7]Seismological Laboratory, California Institute of Technology, Pasadena, CA 91125, USA

Contents of this file

1. Tables S1 to S2
2. Figures S1 to S8
3. Movies S1 to S3 (additionally attached)

Total Moment Tensor	Component-I	Component-II	Component-III
			
	56% DC	44% CLVD	
	NP1=(172.2°, 74.0°, -24.8°)	NP1=(87.6°, 85.5°, -168.9°)	
	NP2=(269.1°, 67.2°, -162.7°)	NP2=(356.7°, 79.0°, -4.6°)	
			
USGS	60% Major DC	40% Minor DC	
NP1=(172°, 74°, -24°)	NP1=(172.2°,74.0°,-23.8°)	NP1=(43.1°,73.0°,-85.2°)	
NP2=(269°, 67°, -163°)	NP2=(269.1°,67.2°,-162.7°)	NP2=(207.1°,17.6°,-105.3°)	
			
	50% Maximum DC	34% Intermediate DC	16% Minimum DC
	NP1=(172.2°,74.0°,-23.8°)	NP1=(338.6°,47.3°,-50.4°)	NP1=(43.1°,73.1°,94.8°)
	NP2=(269.1°,67.2°,-162.7°)	NP2=(108.0°,55.5°,-124.6°)	NP2=(207.1°,17.6°,74.7°)

Table S1: Moment tensor decomposition results for the point-source *W*-phase solution from the USGS-NEIC using different schemes. From top to bottom are double-couple (DC) and compensated linear vector dipole (CLVD), major and minor double-couples, as well as maximum, intermediate and minimum double-couples. The strike, dip, rake of the nodal planes (NP1 and NP2) are listed below the beachballs.

		Hypocenter latitude (°N)	Hypocenter longitude (°W)	Hypocenter depth (km)	Strike(°)	Dip(°)	Subfault along strike, #, size	Subfault along dip, #, size
Single fault		44.465	115.118	10.0	172.3	70.0	15, 4 km	6, 4 km
Two faults	F1	44.333	115.180	13.0	162.9	74.0	8, 4.5 km	7, 3 km
	F2	44.348	115.208	1.23	336.4	60.0	7, 4.5 km	7, 2.9 km

Table S2: Model parameters used in teleseismic finite-fault inversion. Single-fault is for the geometry as shown in Fig. S2, and two-fault is for the geometry as shown in Fig. 3.

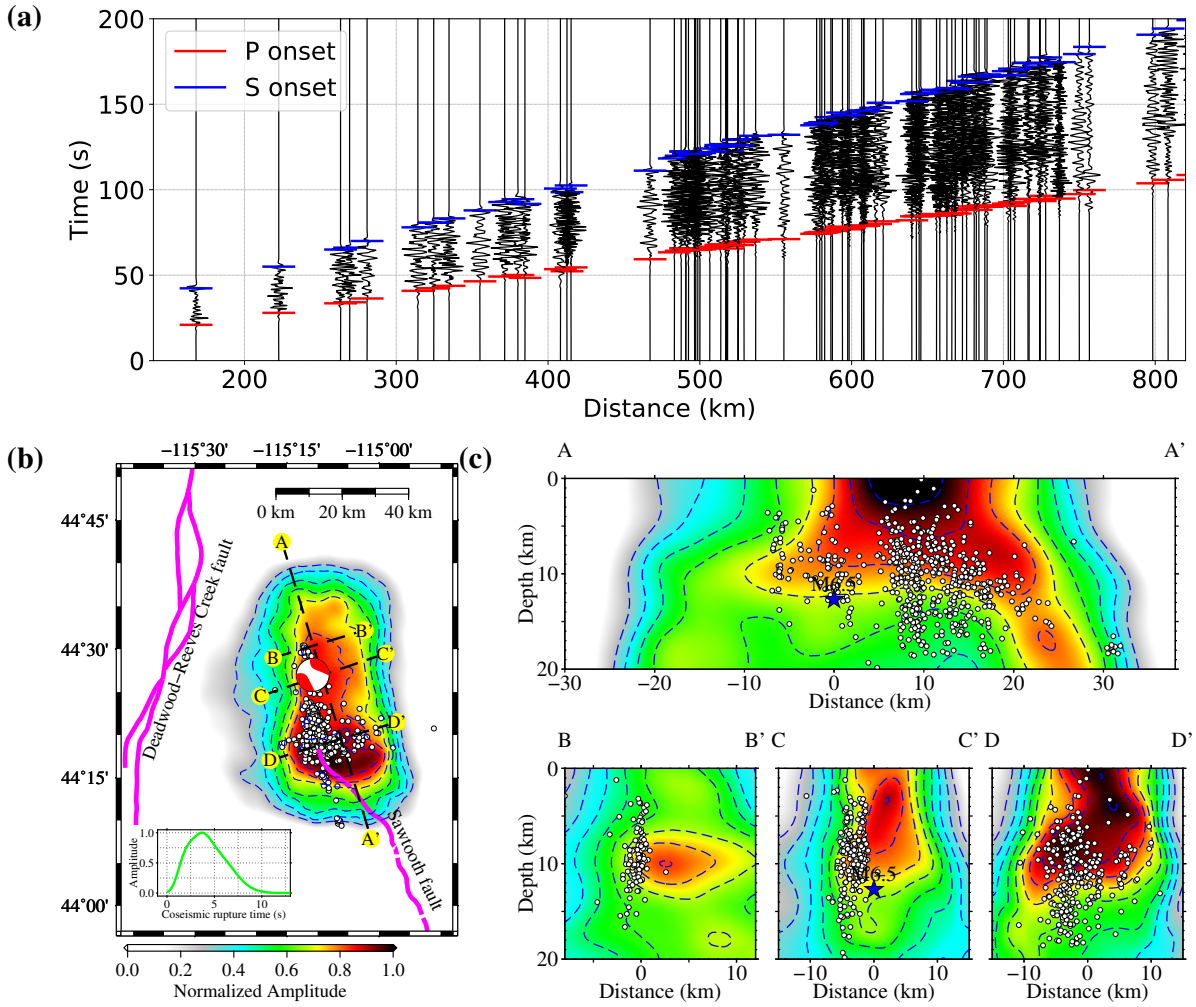

Fig. S1. Normalized cumulative radiated energy calculated with regional multi-azimuth back-projection. (a) Processed regional P-wave records. Blue and red vertical bars denote the P and S-wave onsets, for which the traveltimes are calculated using the fast marching method (Sethian & Popovici, 1999) in a 3D crustal velocity model (Shen & Ritzwoller, 2016). (b) and (c) are normalized cumulative radiated energy in map view and along four vertical profiles, respectively. White dots are the projection of relocated aftershocks in map view and vertical profiles. Note that the distribution of aftershocks is largely anti-correlated with high radiated energy.

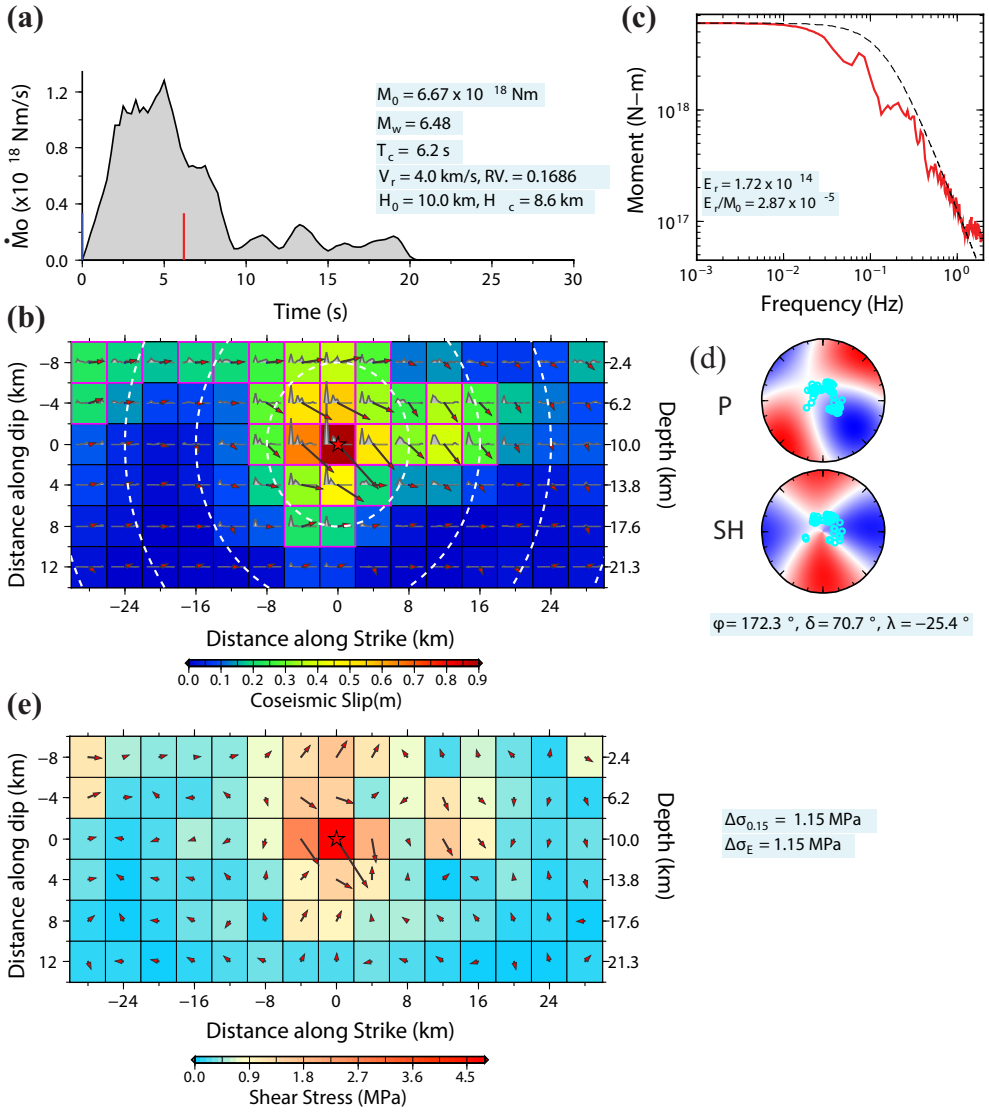

Fig. S2. A single-fault kinematic slip model for the 2020 Stanley earthquake. (a) The moment rate function, along with seismic moment M_w, centroid time T_c (red tick on the time line), imposed kinematic maximum rupture speed V_r, residual variance RV, hypocenter depth H_0 and slip centroid depth H_c. (b) Slip distribution with the average rakes of each subfault patch (vector directions), slip magnitude (vector length and color scale). White dashed lines are 2-s isochrones for the maximum rupture velocity. (c) Source spectrum estimated from the moment rate function spectrum below 0.05 Hz and from stacking of P-wave spectra (after correction for radiation pattern and propagation effects) above 0.05 Hz. E_R denotes radiated energy, and E_R/M_0 denotes moment scaled radiated energy. (d) Lower hemisphere radiation patterns for P and SH waves. Red and blue are compressional and dilational quadrants for P waves, and are clockwise and counter-clockwise quadrants for SH-waves. (e) Shear stress change for the slip model in (b) for a half-space model. $\Delta\sigma_{0.15}$ is the area-truncated circular slip stress drop. $\Delta\sigma_E$ is the slip-weighted stress drop.

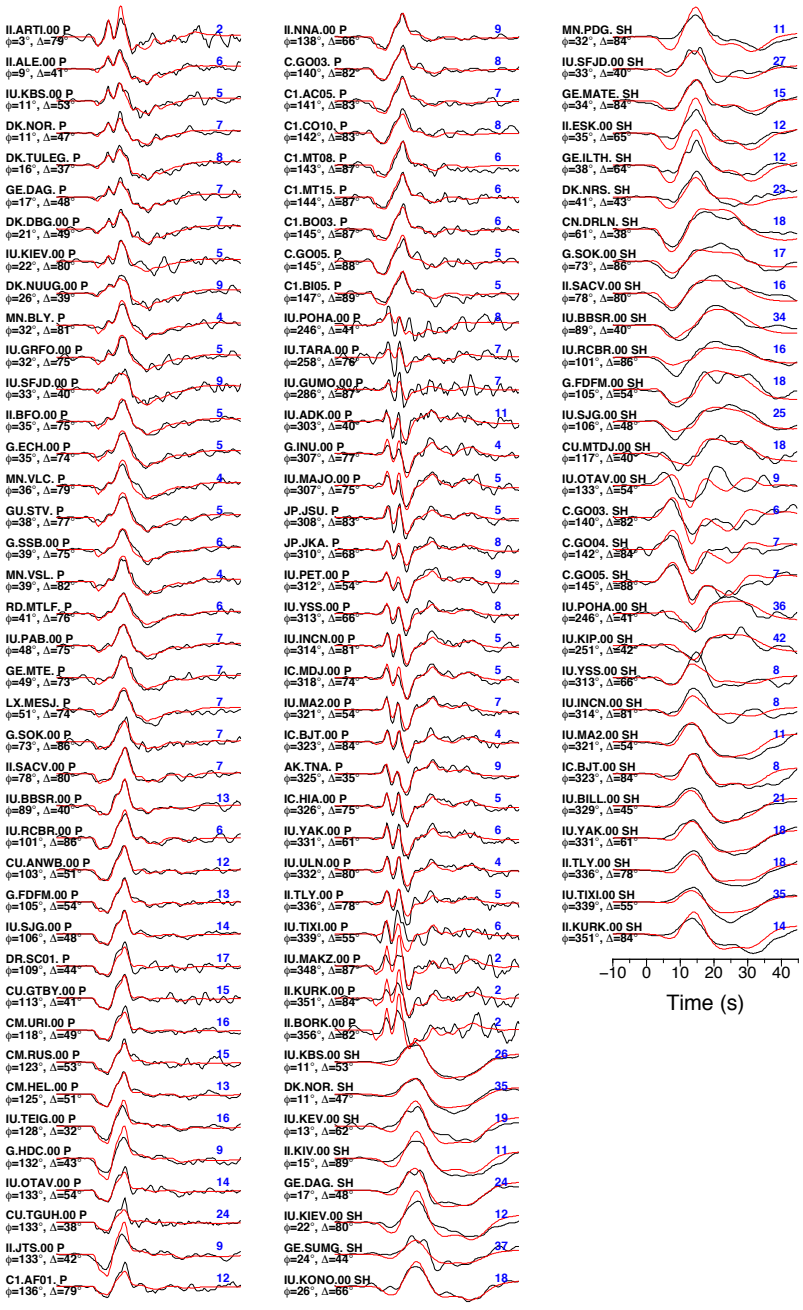

Fig. S3. Comparisons of observed (black) and predicted (red) waveforms for the single-fault slip model shown in Fig. S2. The station names, phase types, along with azimuth and epicenter distances are shown to the left of each comparison. The peak-to-peak amplitude of the data in microns is shown in blue on the right hand side.

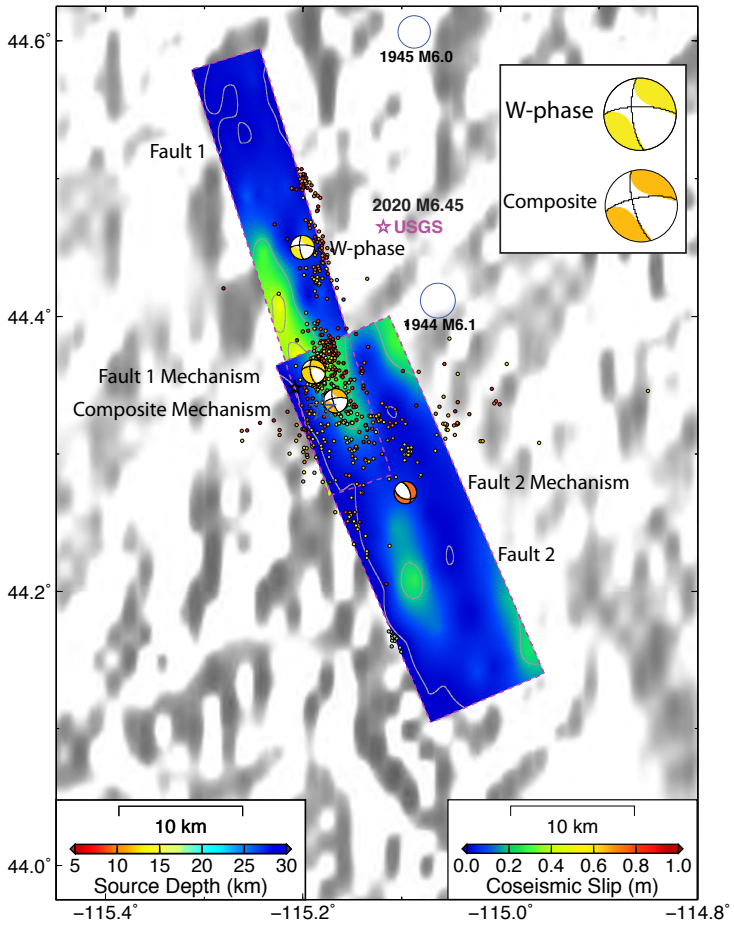

Fig. S4. Map view of the slip model shown in Fig. 3. The magenta star denotes the USGS-NEIC epicenter. The solution from our *W*-phase inversion is shown at its centroid location. The average radiation patterns for the two faults and a composite faulting are shown. Note the similarity of the *W*-phase and composite faulting mechanisms. The relocated aftershocks within one month after the mainshock are superimposed on the slip model. Locations of historic large nearby events are shown by circles with labeled dates.

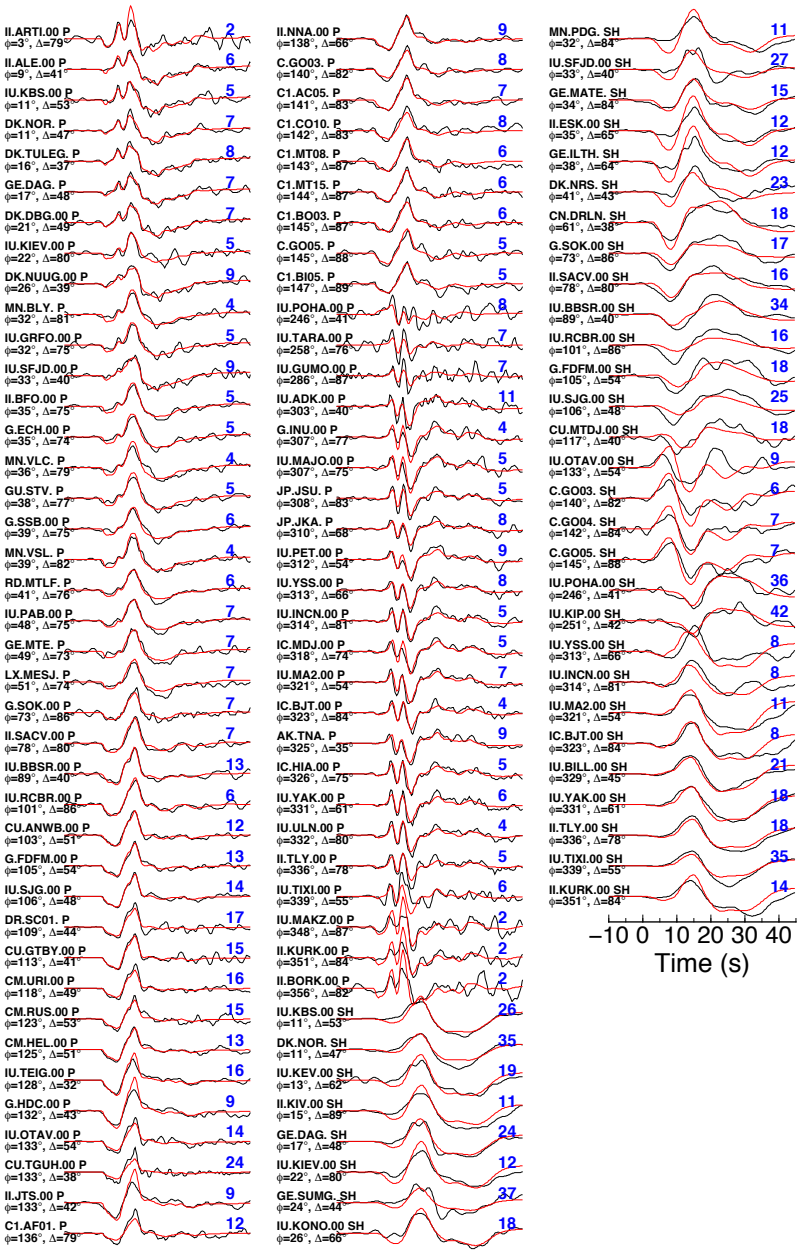

Fig. S5. Comparisons of observed (black) and predicted (red) waveforms for the two-fault slip model shown in Fig. 3. The station names, phase types, along with azimuth and epicenter distances of 72 P and 37 SH phases are shown to the left of each comparison. The peak-to-peak amplitude of the data in microns is shown in blue on the right hand side.

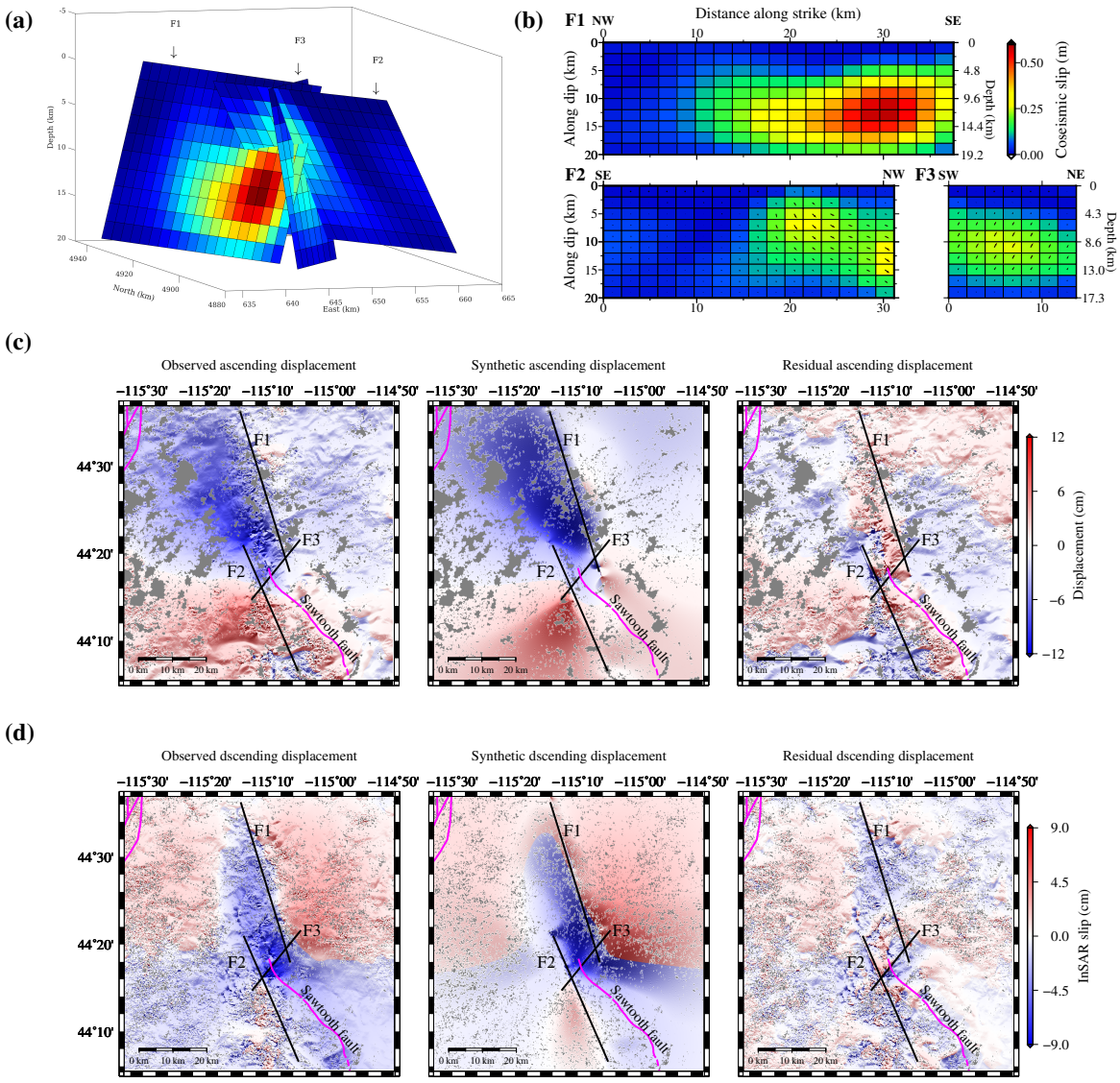

Fig. S6. InSAR analysis results for a three-fault slip model. A third fault about 10 km long is added to the step-over region of the two-fault model shown in Fig. 4. The panel setting is the same as Fig. 4. Note that the third fault has predominantly thrust slip, and the overall maximum slip magnitude is reduced after adding the third fault.

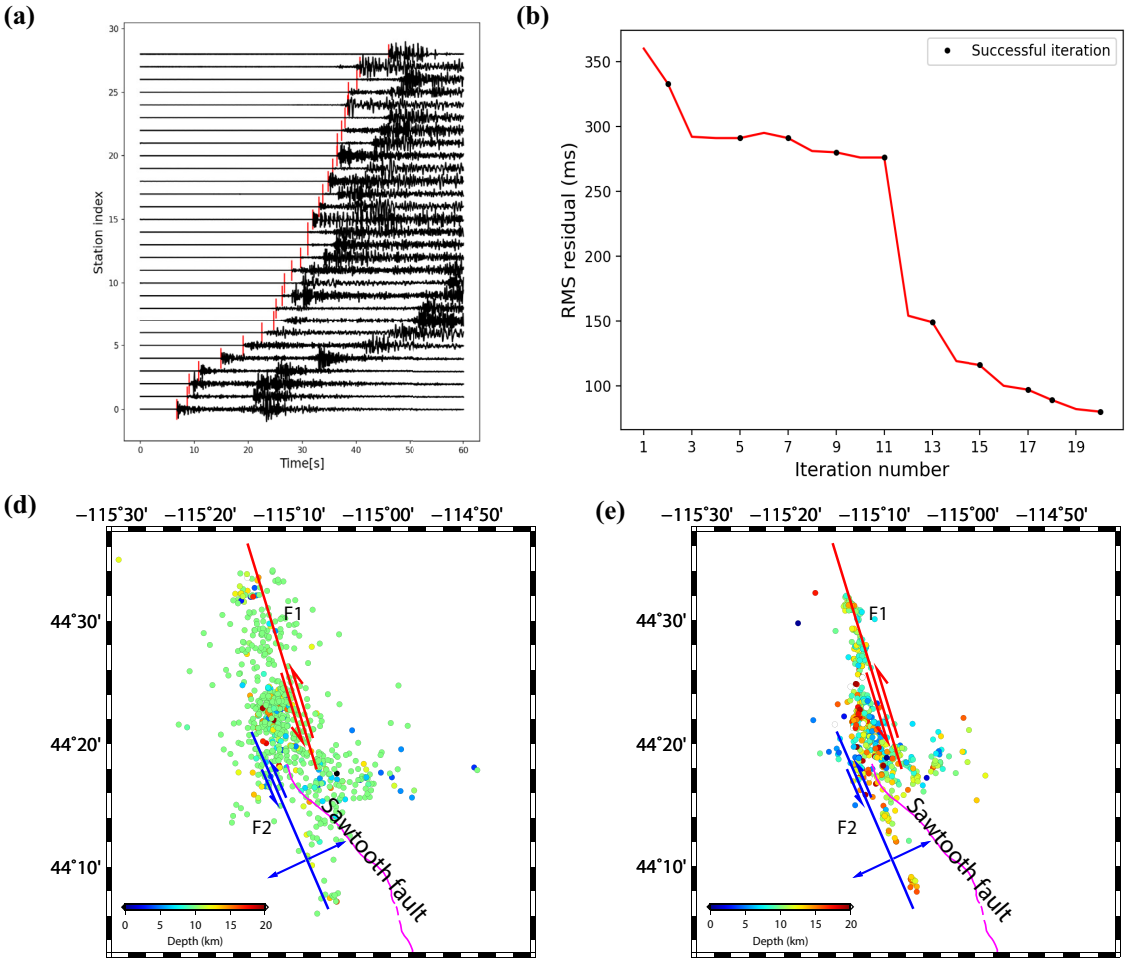

Fig. S7. Relocated aftershocks within one month after the mainshock using a deep-learning-assisted double-difference method. (a) Picked P-wave onsets for a representative event using a deep-learning approach (Ross et al., 2018). (b) Root-mean-square (RMS) residuals of the double-difference travel-time misfit at different iterations. (c) Aftershock location from the USGS-NEIC catalog. (d) double-difference relocated results. Note that significant residual reduction is achieved after the outliers are removed in the first five iterations. The relocated aftershocks in (d) are more focused than those from the USGS-NEIC catalog.

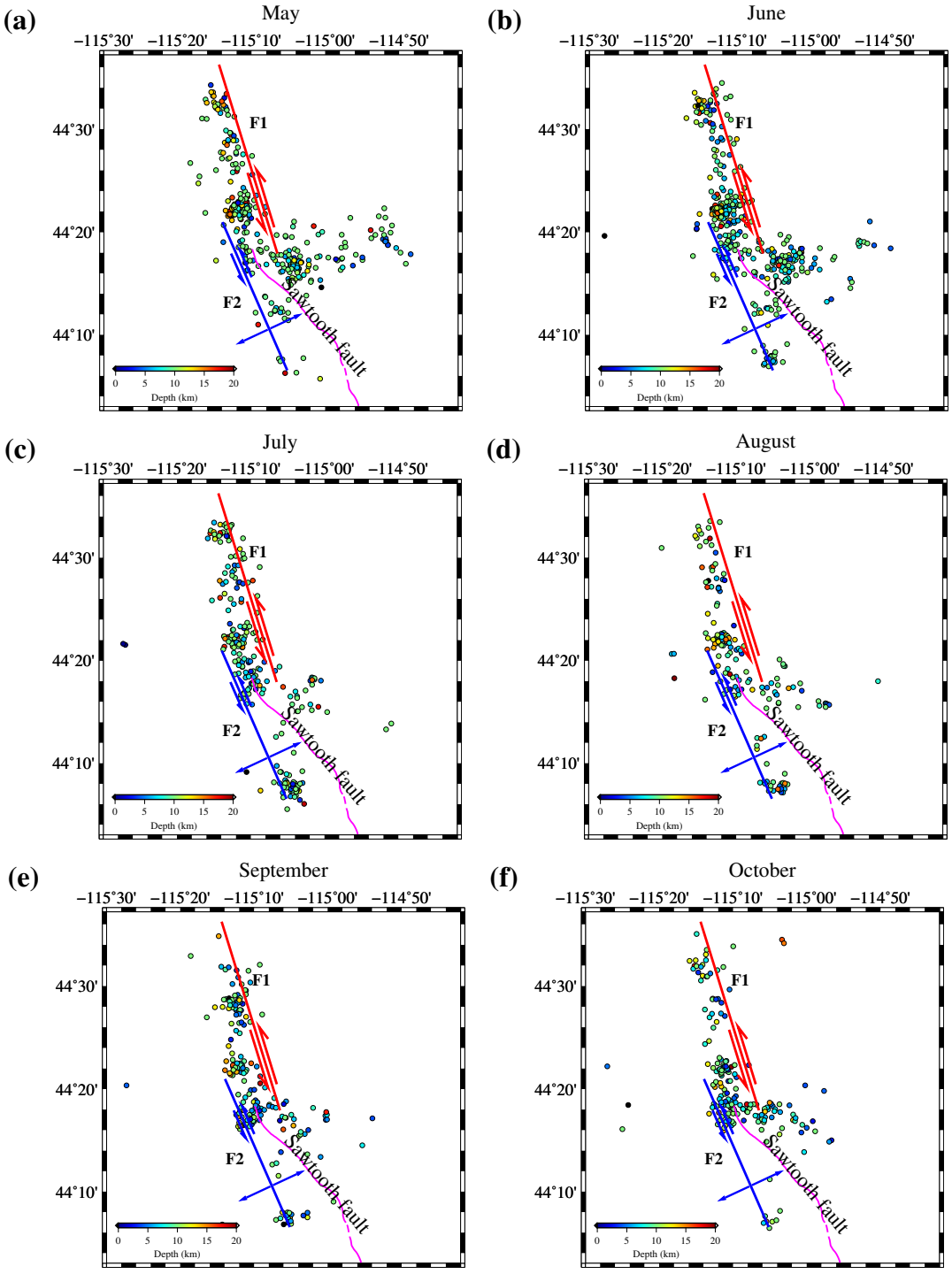

Fig. S8. Evolution of aftershocks from May to October, 2020, downloaded from the USGS-NEIC catalog.

Movie S1. Coseismic rupture propagation imaged from regional multi-azimuth back-projection analysis. The results show that the earthquake first ruptured an unmapped northern subfault F1, then changed to move southwestward (the step-over region), and finally ruptured a southern subfault F2 sub-parallel to the Sawtooth fault scarp.

Movie S2. A 3D slip model computed by finite-fault inversion overlapped with relocated aftershocks (black dots) from different views.

Movie S3. A 3D slip model computed by InSAR analysis overlapped with relocated aftershocks (black dots) from different views.

References

Ross, Z. E., Meier, M.-A., & Hauksson, E. (2018). P Wave Arrival Picking and First-Motion Polarity Determination With Deep Learning. *Journal of Geophysical Research: Solid Earth*, *123*(6), 5120-5129. doi: 10.1029/2017JB015251

Sethian, J. A., & Popovici, A. M. (1999). 3-D traveltime computation using the fast marching method. *Geophysics*, *64*(2), 516-523.

Shen, W., & Ritzwoller, M. H. (2016). Crustal and uppermost mantle structure beneath the United States. *Journal of Geophysical Research: Solid Earth*, *121*(6), 4306–4342.